

Journal of  
**Applied Remote Sensing**

RemoteSensing.SPIEDigitalLibrary.org

## **Improving remotely sensed fused ocean data products through cross- sensor calibration**

Mark David Lewis  
Ruhul Amin  
Sonia Gallegos  
Richard W. Gould, Jr.  
Sherwin Ladner  
Adam Lawson  
Rong-rong Li

# Improving remotely sensed fused ocean data products through cross-sensor calibration

Mark David Lewis,<sup>a,\*</sup> Ruhul Amin,<sup>a</sup> Sonia Gallegos,<sup>a</sup>  
Richard W. Gould Jr.,<sup>a</sup> Sherwin Ladner,<sup>a</sup>  
Adam Lawson,<sup>a</sup> and Rong-rong Li<sup>b</sup>

<sup>a</sup>Naval Research Laboratory, Code 7331, Building 1009, Stennis Space Center,  
Mississippi 39529, United States

<sup>b</sup>Naval Research Laboratory, Code 7231, Building 2, Washington, DC 20375, United States

**Abstract.** Standard oceanographic processing of the visible infrared imaging radiometer suite (VIIRS) and the moderate resolution imaging spectroradiometer (MODIS) data uses established atmospheric correction approaches to generate normalized water-leaving radiances ( $nLw$ ) and bio-optical products. In many cases, there are minimal differences between temporally and spatially coincident MODIS and VIIRS bio-optical products. However, due to factors such as atmospheric effects, sensor, and solar geometry differences, there are cases where the sensors' derived products do not compare favorably. When these cases occur, selected  $nLw$  values from one sensor can be used to vicariously calibrate the other sensor. Coincident VIIRS and MODIS scenes were used to test this cross-sensor calibration method. The VIIRS sensor was selected as the "base" sensor providing "synthetic" *in situ*  $nLw$  data for vicarious calibration, which computed new sensor gain factors used to reprocess the coincident MODIS scene. This reduced the differences between the VIIRS and MODIS bio-optical measurement. Chlorophyll products from standard and cross-sensor calibrated MODIS scenes were fused with the VIIRS chlorophyll product to demonstrate the ability for this cross-sensor calibration and product fusion method to remove atmospheric and cloud features. This cross-sensor calibration method can be extended to other current and future sensors. © The Authors. Published by SPIE under a Creative Commons Attribution 3.0 Unported License. Distribution or reproduction of this work in whole or in part requires full attribution of the original publication, including its DOI. [DOI: [10.1117/1.JRS.9.095063](https://doi.org/10.1117/1.JRS.9.095063)]

**Keywords:** vicarious calibration; cross-sensor calibration; remote sensing; visible infrared; imaging radiometer suite; moderate resolution imaging; spectroradiometer.

Paper 15163 received Mar. 3, 2015; accepted for publication Jun. 16, 2015; published online Jul. 23, 2015.

## 1 Introduction

The moderate resolution imaging spectroradiometer (MODIS) on the Terra satellite has been operational since 1999, and the MODIS sensor on the Aqua satellite since 2002.<sup>1</sup> The visible infrared imaging radiometer suite (VIIRS) on the Suomi National Polar-orbiting Partnership (SNPP) satellite was launched in 2012.<sup>2</sup> VIIRS is continuing the legacy of earth and ocean observations established by MODIS, the sea-viewing wide-field-of-view sensor (SeaWiFS),<sup>3</sup> and the coastal zone color scanner.<sup>4</sup>

For satellite-based earth observing sensors, accurate radiometric measurements are required to correctly derive in-water ocean properties. Laboratory radiometric calibration performed prior to launch enables the sensor-measured digital counts to be converted into radiance units. Thus, after launch these sensors provide total radiance ( $L_t$ ) measurements at the top of the atmosphere. Because the  $L_t$  over the ocean is dominated by atmospheric radiances and the radiances from the ocean are low, particularly relative to radiances from land targets, accurate atmospheric correction is required to derive water-leaving radiance ( $L_w$ ) from the  $L_t$  values. These  $L_w$  values are normalized using the solar zenith angle, diffuse transmittance, bi-directional reflectance

---

\*Address all correspondence to: Mark David Lewis, E-mail: [dlewis@nrlssc.navy.mil](mailto:dlewis@nrlssc.navy.mil)

correction, spectral bandpass effects, and the Earth–Sun distance to yield normalized water-leaving radiance ( $nLw$ ) values, which are divided by the solar irradiance to calculate remote sensing reflectance ( $Rrs$ ). The  $nLw$  and  $Rrs$  values are used in various bio-optical inversion algorithms to estimate in-water biogeochemical and optical properties.<sup>5</sup>

Over time, the sensitivity of a satellite sensor can degrade, causing the current relationship between the sensor's recorded digital count and true total radiance to differ from what was measured before launch in a stable laboratory environment. Thus, there is a need to continuously examine and adjust the sensor calibration. This can be done using a variety of methods, including solar and lunar viewing. Vicarious calibration,<sup>6</sup> which can also be used to adjust a sensor's calibration, is a system correction that uses *in situ* measurements to calculate sensor gain factors. When applied to the sensor's  $Lt$  values these gain factors fine-tune the results of the radiometric calibration, thereby improving the accuracy of satellite retrievals. Vicarious calibration corrects for aggregated confounding influences including the differences between the laboratory radiometric calibration and required calibration for space operations, degradation of the sensor over time, atmospheric correction errors, and geometric and environmental factors.

Kwiatkowska et al.<sup>7</sup> applied a vicarious calibration to MODIS Terra based on SeaWiFS data as an instrument characterization approach to respond to the MODIS Terra temporal drift in measuring the blue wavelength bands. Multiple dates of imagery were used to generate adjustments to the standard MODIS Terra gains using SeaWiFS data, demonstrating that a vicarious calibration approach can be used to perform cross-calibration for scene pairs when the sensors' are not generating similar bio-optical values over the same water masses.

Wang and Franz<sup>8</sup> discussed a vicarious intercalibration approach for the modular optoelectronic scanner (MOS) using SeaWiFS data based on reflectance data from two scene pairs. The resulting sensor gains were then applied to other MOS scenes, generating  $nLw$  values that compared favorably with the coincident SeaWiFS  $nLw$  values. If differences between the  $nLw$  values of the MODIS and VIIRS sensors occur that cause artifacts in fused product of the resulting bio-optical products, a vicarious calibration process using  $nLw$  measurements could be used to resolve these differences. Franz et al.<sup>9</sup> discuss the vicarious calibration process for SeaWiFS were *in situ* data from the Marine Optical Buoy (MOBY),<sup>10</sup> moored near the Hawaiian island of Lanai provides  $Lw$  measurements continuously over time for use as the *in situ* data in the vicarious calibration process. Initially, the satellite sensor gain factors for each wavelength band are set to a default value. During the vicarious calibration process, the sensor gain factors are adjusted using the *in situ* MOBY  $Lw$  data and applied as a multiplicative factor to the satellite  $Lt$  values resulting in an improvement in the derived  $Lw$  and  $nLw$  measurement accuracy.

The Aqua and SNPP satellites are polar orbiting and fly in a coordinated group of satellites called the A-Train.<sup>11,12</sup> SNPP follows Aqua as these satellites cross the equator northbound at about 1:30 pm local time within a few minutes of each other. The proximity in these sensors' orbits provides many nearly coincident overlapping areas of interest within the sensor's field of view. Because of the wide swath width of these sensors, there are also cases when an area of interest within the extent of one sensor's current orbit is also in the extent of the other sensor's previous orbit. In these cases, VIIRS and MODIS scenes over the same extent are often acquired within 90 min of each other. The short difference in acquisition times enables direct comparison of the derived  $nLw$  values for the two sensors at the same geographic location. However, the time difference between the sensors' acquisitions in many cases is large enough to allow clouds that cover locations in the first scene to move and expose these locations to the satellite sensor in the second scene. This provides the possibility of creating a scene with reduced cloud cover by fusing the two scenes.

Due to the accurate radiometric calibration and consistent atmospheric correction; in many cases, there is little difference between the  $nLw$  values from coincident VIIRS and MODIS scenes. However, in some cases, there are differences between the  $nLw$  estimates derived from VIIRS and MODIS, primarily in the blue wavelength bands. There are several reasons that can contribute to the sensor  $nLw$  differences. It is possible that the moving solar geometry might create differences in total radiance measurements between the times of the sensors' acquisitions. Also, for some scene pairs, the atmospheric correction algorithm might perform better for one sensor than it does for another sensor. Factors that can contribute to the difference in

algorithm performance include differences in solar and viewing angles between the scenes and also changes in the atmospheric haze or aerosol distribution during the time between scene acquisitions. This might lead to differences in the aerosol models selected during the scenes' atmospheric correction, which can result in differences in their derived  $nLw$  values.

Since data from one or both sensors may have cloud obstruction or other anomalous effects such as sun glint, the availability of multiple scenes over the same area reasonably close in time provides the opportunity to fuse the scenes together to remove these effects. This fusion allows data from one sensor with clearer cloud-free pixels to replace cloud-contaminated data from another sensor. Hence, when cloud contamination occurs, a clearer scene of combined sensor derived data values can be created from multiple partially cloudy scenes. Therefore, for many bio-optical products this provides the ability to create a fused image which has fewer pixels affected by atmospheric correction failures or cloud cover than any of the individual overlapping scenes. However, to create an optimal scene fusion, the estimated values of the data products from the multiple sensors involved in the fusion must be consistent.

Whereas the vicarious calibration method is often used to establish sensor gains based on *in situ* data measurements, it can also be used to cross-calibrate one sensor based on data from another sensor. This cross-sensor calibration can be performed as a special case of vicarious calibration, where data from one sensor provides "synthetic" *in situ* data as a proxy for the actual *in situ* measurements used to vicariously calculate updated sensor gain factors for the second sensor. Therefore, when differences between the  $nLw$  values of sensors such as VIIRS and MODIS are observed, selected  $nLw$  values from one sensor can be used to perform cross-sensor calibration for the other sensor, which leads to closer agreement in derived values between the sensors and creates an improvement in the fused products. Thus, the cross-sensor calibration computes adjusted gain factors for each band such that the differences between the estimated  $nLw$  values of each sensor are minimized, resulting in closer agreement between the sensors' derived bio-optical data products generated from the  $nLw$ .

## 2 Methods and Data

There is a distinction between the sensors involved in the cross-sensor calibration process. Let the sensor that is providing the synthetic *in situ* data be called the "base" sensor. Let the sensor that results in adjusted gain factors be called the "calibrated" sensor. This study uses VIIRS as the base sensor and MODIS as the calibrated sensor; although we examine only these two sensors, other sensors, such as the future Sentinel-3 Ocean and Land Colour Imager,<sup>13</sup> could also be included as a base or calibrated sensor in future cross-sensor calibration and scene fusion activity.

Performing the cross-sensor calibration at locations and on dates that have cloud contamination provides extended coverage intended to more effectively fill in obscured areas in one scene with cloud-free data from another scene. The cross-sensor calibration method was performed using VIIRS and MODIS scene pairs, and then the scenes were fused together to reduce cloud contamination.

The focus of this investigation is to fuse the two data sources into a single, consistent dataset, not to determine which sensor is more accurate. Therefore, no actual *in situ* data were used to evaluate whether the VIIRS or MODIS  $nLw$  values were more accurate. Therefore, either sensor could have been selected as the base sensor. However, the Aqua and Terra MODIS sensors are passed their expected lifetimes and over the years, the MODIS science team has been responding to degradation in these sensors' blue wavelength bands.<sup>14</sup> Also, the VIIRS sensor is at the beginning of its life expectancy and is positioned to continue the legacy of MODIS earth observation into the future. Therefore, VIIRS was selected as the base sensor and provided the synthetic *in situ*  $nLw$  data. The vicarious calibration process resulted in scene-dependent adjustments to the MODIS gain factors for each band to minimize the derived  $nLw$  differences between the VIIRS and the MODIS (calibrated sensor) data. Although this study specifically explores the cross-sensor calibration methodology for the VIIRS and MODIS sensors, the methodology can naturally be extended to include other sensors. The cross-sensor calibration methodology will be referred to as "cross-calibration" to simplify the rest of this text.

## 2.1 Theoretical Background

The automated processing system (APS),<sup>15</sup> developed at the Naval Research Laboratory (NRL), was used to process the VIIRS and MODIS data. APS is based on and is consistent with the NASA SeaWiFS Data Analysis System (SeaDAS).<sup>16</sup> Therefore, it uses established atmospheric correction and bio-optical algorithms endorsed by the ocean color community.<sup>5</sup> APS extends the SeaDAS functionality by adding a batch processing capability to rapidly reprocess many data files and incorporates the capability to add and test new algorithms. APS generates a standard set of bio-optical image products, including chlorophyll concentration, water absorption, and backscattering coefficients.

In addition to the standard forward pass through the atmospheric correction process, the vicarious calibration process uses an inverse pass that has been incorporated into SeaDAS and APS. Together, the forward and inverse passes of the atmospheric correction process provide the required vicarious calibration information. This process has been comprehensively described by Bailey et al. and Franz et al.,<sup>6,7</sup> so only a brief description relevant to the cross-calibration activity will be presented here. The  $\lambda$  parameter in the following equations denotes an individual wavelength of a radiance term. When the radiance term is used without the  $\lambda$  parameter it refers to all the wavelengths of the radiance term collectively in one symbol.

In general, during the atmospheric correction process, the  $L_t$  is broken into terms represented by

$$L_t(\lambda) = [L_r(\lambda) + L_a(\lambda) + t_{dv}(\lambda)L_{wc}(\lambda) + t_{dv}(\lambda)L_w(\lambda)]t_{gv}(\lambda)t_{gs}(\lambda)f_p(\lambda), \quad (1)$$

where  $L_t(\lambda)$ ,  $L_r(\lambda)$ ,  $L_a(\lambda)$ ,  $L_{wc}(\lambda)$ , and  $L_w(\lambda)$  represent the total radiance at the top of the atmosphere, its radiance components associated with Rayleigh scattering, atmospheric aerosols, surface whitecaps (sea foam), and water and the  $t_{dv}(\lambda)$ ,  $t_{gv}(\lambda)$ ,  $t_{gs}(\lambda)$  and  $f_p(\lambda)$  terms represent diffuse transmittance along the sensor view path from the surface to the satellite, account for losses due to gaseous absorption along the radiant paths from the Sun to the surface and the surface to the sensor and a correction for instrument response to the polarization of the observed radiance as functions of the wavelength,  $\lambda$ .<sup>6,7</sup> During the forward pass through the atmospheric correction,  $L_r(\lambda)$  and  $L_{wc}(\lambda)$  are computed in part from tables indexed by the solar and sensor geometries.<sup>17</sup>  $L_a(\lambda)$  is computed using the Gordon and Wang aerosol model selection method<sup>18</sup> which selects the appropriate aerosol model based on atmospheric correction parameters characterized by two near-infrared (NIR) wavelength bands.

Equation (1) can be inverted, resulting in

$$L_w(\lambda) = \left\{ \left[ \frac{L_t(\lambda)}{t_{gv}(\lambda)t_{gs}(\lambda)f_p(\lambda)} \right] - [L_r(\lambda) + L_a(\lambda) + t_{dv}(\lambda)L_{wc}(\lambda)] \right\} \left[ \frac{1}{t_{dv}(\lambda)} \right]. \quad (2)$$

The  $L_t(\lambda)$  term is measured by the satellite sensor and after the  $r(\lambda)$ ,  $L_a(\lambda)$ ,  $L_{wc}(\lambda)$ ,  $t_{dv}(\lambda)$ ,  $t_{gv}(\lambda)$ ,  $t_{gs}(\lambda)$ , and  $f_p(\lambda)$  terms in Eq. (2) are computed in the forward pass of the atmospheric correction, the derived  $L_w(\lambda)$  value can then be calculated. Furthermore, the normalized  $nL_w$  can then be computed by

$$nL_w(\lambda) = L_w(\lambda)/(\mu_s f_s t_{ds} f_b f_\lambda), \quad (3)$$

where  $\mu_s$  is the cosine of the solar zenith angle,  $f_s$  adjusts for changes in Earth–Sun distance,  $t_{ds}$  accounts for the diffuse transmittance along the sensor view path from the sun to the surface,  $f_b$  is a surface bidirectional reflectance correction, and  $f_\lambda$  accounts for the spectral bandpass effects. In this calibration work, all these terms are associated with the MODIS sensor, since it is the sensor to be calibrated.

Equation (3) can be inverted, resulting in

$$L_w(\lambda) = nL_w(\lambda) \cdot (\mu_s f_s t_{ds} f_b f_\lambda). \quad (4)$$

The inverse pass allows for  $L_w(\lambda)$  values derived from the synthetic *in situ*  $nL_w(\lambda)$  measurements to replace the satellite-derived  $L_w(\lambda)$  values at an *in situ* sample point location. Equation (4) can be used to compute the calibrated sensor's (MODIS) *in situ* water-leaving

radiance value,  $Lw(\lambda)_{in\ situ}$  based on the base sensor's (VIIRS) synthetic *in situ* normalized water-leaving radiance value,  $nLw(\lambda)_{in\ situ}$  by

$$Lw(\lambda)_{in\ situ} = nLw(\lambda)_{in\ situ} \cdot (\mu_s f_s t_{ds} f_b f_\lambda). \quad (5)$$

The inverse pass then can add the already computed atmospheric correction radiance values to the  $Lw(\lambda)_{in\ situ}$  value in order to generate a new  $vLt(\lambda)$  value, which is the vicariously calibrated total radiance at the top of the atmosphere. Therefore, by using the form of Eq. (1), the  $vLt(\lambda)$  can be computed by

$$vLt(\lambda) = [Lr(\lambda) + La(\lambda) + t_{dv}(\lambda) Lwc(\lambda) + t_{dv}(\lambda) Lw(\lambda)_{in\ situ}] t_{gv}(\lambda) t_{gs}(\lambda) f_p(\lambda). \quad (6)$$

Therefore, the forward pass establishes the values for the  $r(\lambda)$ ,  $La(\lambda)$ ,  $Lwc(\lambda)$ ,  $t_{dv}(\lambda)$ ,  $t_{gv}(\lambda)$ ,  $t_{gs}(\lambda)$ , and  $f_p(\lambda)$  terms, while the inverse pass uses the base sensor's  $nLw(\lambda)_{in\ situ}$  value to generate the calibrated sensor's  $Lw(\lambda)_{in\ situ}$  term. During the inverse pass, all the calibrated sensor's radiance terms are used to compute the  $vLt(\lambda)$  value. The ratio of the  $vLt(\lambda)$  and  $Lt(\lambda)$ , computed by

$$\text{gain}_{vc}(\lambda) = \frac{vLt(\lambda)}{Lt(\lambda)}, \quad (7)$$

yields gain factors for the calibrated sensor's (MODIS) wavelength bands. Inverting Eq. (7), results in

$$vLt(\lambda) = Lt(\lambda) \cdot \text{gain}_{vc}(\lambda). \quad (8)$$

Therefore, the product of the  $Lt(\lambda)$  and  $\text{gain}_{vc}(\lambda)$  results in a  $vLt(\lambda)$  value which is the total radiance value required such that after the atmospheric correction the derived  $nLw(\lambda)$  value of the calibrated sensor matches the base sensor's synthetic *in situ*  $nLw(\lambda)$  value.

Assume that  $vLt(\lambda)$  is generated at several synthetic *in situ* sample point locations. Then, the new unweighted vicariously calibrated gains can be computed with

$$\text{gain}_{vc_{\text{mean}}}(\lambda) = \frac{\left( \sum_{i=1}^n \frac{vLt_i(\lambda)}{Lt_i(\lambda)} \right)}{n}, \quad (9)$$

where  $n$  is the number of *in situ* sample points. Finally, the new cross-calibrated gains can be generated by multiplying the unweighted vicariously calibrated gains with the currently used standard sensor gains, denoted as

$$\text{gain}_{\text{cross calibrated}}(\lambda) = \text{gain}_{vc_{\text{mean}}}(\lambda) \cdot \text{gain}_{\text{standard}}(\lambda), \quad (10)$$

where  $\text{gain}_{\text{standard}}(\lambda)$  represents the currently used standard sensor gains for the calibrated sensor.

When the calibrated sensor data are reprocessed applying these cross-calibrated gains to the radiometrically calibrated  $Lt$  data, the differences between the resulting calibrated sensor (MODIS)  $nLw$  data and the base sensor (VIIRS)  $nLw$  data at the sample point locations are minimized, thereby fine-tuning the calibrated sensor to approximate the base sensor  $nLw$  values at the sample points. If the sample point locations sufficiently represent the distribution of data across the scene, these same cross-calibrated gains will bring the  $nLw$  estimates of the two sensors into agreement across the scene extent.

## 2.2 Cross-Calibration for Chesapeake Bay and Mississippi Bight Study Locations

The overall objective of this work is to use vicarious calibration to adjust the MODIS  $nLw$  data so that they more closely match the VIIRS  $nLw$  data, and then fuse the VIIRS and cross-calibrated MODIS chlorophyll products to remove as much cloud contamination as possible. The cross-calibration methodology, which was applied to two different VIIRS and MODIS scene pair

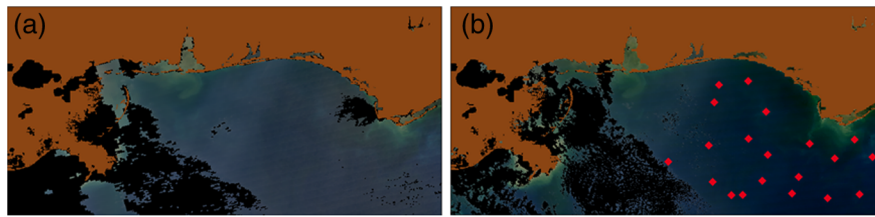


**Fig. 1** Mississippi Bight March 14, 2014: true color (a) moderate resolution imaging spectroradiometer (MODIS), (b) visible infrared imaging radiometer suite (VIIRS) with *in situ* points marked in red.

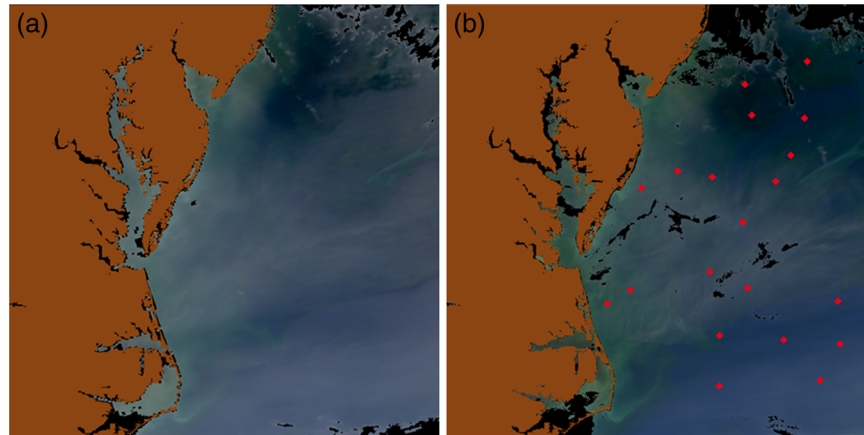


**Fig. 2** Chesapeake Bay May 17, 2013: true color (a) MODIS and (b) VIIRS with *in situ* points marked in red.

study areas, generated cross-calibrated gains for MODIS, which were used to reprocess the MODIS scenes. Derived products taken before and after the cross-calibration were compared to assess the improvement of the cross-calibration.

The scenes from the first study area over the Mississippi Bight in the northern Gulf of Mexico were acquired on March 14, 2014. The true color MODIS image for the Mississippi Bight is shown in Fig. 1(a) and the true color VIIRS image, with the location of its associated 20 synthetic *in situ* sample points, is shown in Fig. 1(b). The scenes from the second study area over the Chesapeake Bay and coastal waters of the Atlantic Ocean were acquired on May 17, 2013. The true color MODIS image for the Chesapeake Bay is shown in Fig. 2(a) and the true color VIIRS image, with the location of its associated 20 synthetic *in situ* sample points, is shown in Fig. 2(b).

When processed with their respective standard gains, the difference between the VIIRS and MODIS  $nLw$  measurements for these scene pairs occur primarily in the blue and green wavelength bands. The chl<sub>oc3</sub> chlorophyll algorithm uses a ratio of blue and green wavelength bands to estimate the chlorophyll value.<sup>19,20</sup> Differences between the VIIRS and MODIS  $nLw$  measurements in these blue and green wavelength bands therefore lead to differences in the computed chl<sub>oc3</sub> chlorophyll product values between the two sensors. As a result, the chlorophyll products are good surrogate images for visually identifying if there are differences between the sensors' derived  $nLw$  values in the blue and green wavelengths. Visual identification of differences in chlorophyll products was used as a screening technique to select the Mississippi Bight and Chesapeake Bay scene pairs.

The VIIRS bands used in this study have a 750-m spatial resolution, while the relevant MODIS bands have a 1-km spatial resolution. Using an APS mapping function, both the VIIRS and MODIS data were georeferenced to a nearest neighbor 750-m spatial resolution geographic grid. This equivalently provided sized image grids for direct comparison between the data products.

**Table 1** Moderate resolution imaging spectroradiometer (MODIS) and visible infrared imaging radiometer suite (VIIRS) wavelengths used in the cross-calibration.

MODIS wavelengths (nm)	412	443	488	531	547	667	678	748	869
VIIRS wavelengths (nm)	410	443	486	531 <sup>a</sup>	551	671	678 <sup>a</sup>	745	862

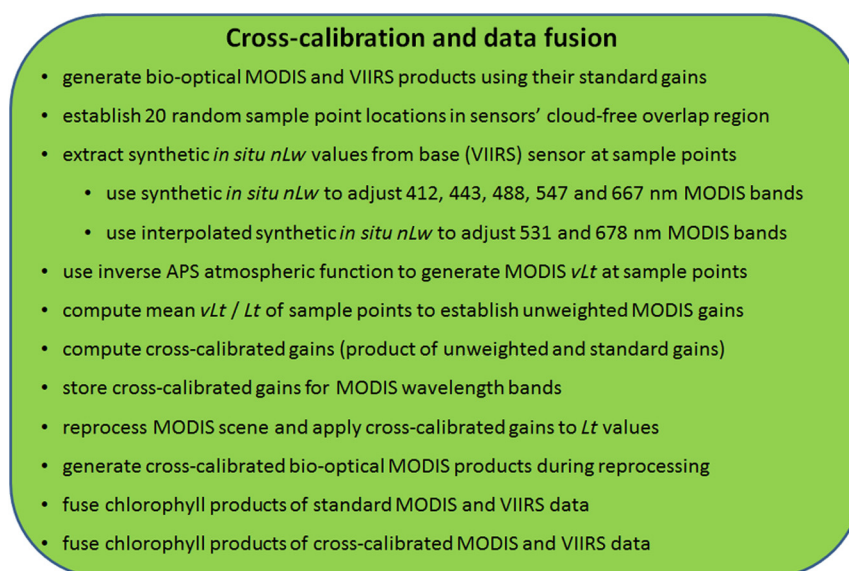
<sup>a</sup>Interpolated between adjacent VIIRS bands

The  $nLw$  value for each VIIRS wavelength at each sample point was extracted to provide the synthetic *in situ*  $nLw$  data for the vicarious calibration process. The location of these points for the Mississippi Bight and Chesapeake Bay study areas is shown in Figs. 1(b) and 2(b), respectively. These synthetic *in situ*  $nLw$  data were used in the APS inverse pass of the atmospheric correction process to generate the vicariously calibrated  $vLt$  values. The mean of the  $vLt/Lt$  values across the samples was computed to create the unweighted cross-calibrated MODIS gains. These gains were multiplied by the standard MODIS gains to generate the cross-calibrated gains.

The VIIRS and MODIS sensors also have different spectral resolutions. Table 1 shows the central wavelengths for the VIIRS and MODIS visible/near-infrared (VNIR) wavelength bands. As the table shows, VIIRS does not have bands associated with the MODIS 531 and 678 nm wavelengths. Therefore, VIIRS  $nLw$  data for the 531 and 678 nm wavelength regions were interpolated from adjacent bands in order to provide synthetic  $nLw$  data for the vicarious calibration process. The process used a linear interpolation between the 486 and 551 nm VIIRS  $nLw$  values to estimate the VIIRS  $nLw$  value at 531 nm. Similarly, it used a linear interpolation between the 671 and 745 nm VIIRS  $nLw$  values to estimate the  $nLw$  value at 678 nm. Whereas the spectral curve in these regions is not typically linear, the absolute values in these regions are small and the interpolation to estimate  $nLw$  values for these wavelength bands provided the measurements needed to perform a comprehensive cross-calibration for all VNIR bands. Since the difference between VIIRS and MODIS wavelength centers is sufficiently small (4 nm or less) across the visible range, no other spectral adjustments were performed. As a result, cross-calibrated gains were generated for the MODIS visible wavelength bands from directly measured or interpolated VIIRS synthetic *in situ*  $nLw$  data.

### 3 Results and Discussion

The steps performed for the cross-calibration and image fusion methodology are shown in Fig. 3. The steps for generating performance metrics to evaluate the results of the cross-calibration are

**Fig. 3** Cross-calibration and image fusion methodology.

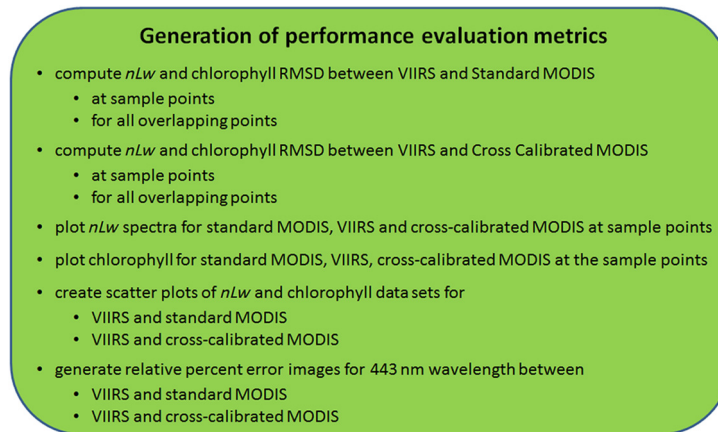


**Fig. 4** Cross-calibration performance metric generation.

shown in Fig. 4. However, these performance metrics might not be required when performing the cross-calibration and data fusion process in an operational mode.

### 3.1 Differences Between Vicarious Calibration for Standard Gains and Cross-Calibrated Gains

There are differences between the vicarious calibration used in this scene dependent cross-calibration study and the broader vicarious calibration used to establish standard sensor gain factors discussed in Franz et al.<sup>7</sup> The most obvious difference is that whereas the broader vicarious calibration uses true *in situ* data provided by in-water sensors, the cross-calibration uses synthetic *in situ* data provided by one of the sensors. Therefore, the cross-calibration is not necessarily minimizing the error between the satellite-derived  $nLw$  values and actual “ground truth”  $nLw$  measurements; it is minimizing the difference between the  $nLw$  values of the two sensors. This implies that the cross-calibration process is not necessarily resulting in satellite-derived values that are closer to the actual environmental truth, only that the derived values from the two sensors are closer to each other. Since our goal is to enforce consistency of bio-optical properties from multiple sensors to improve their fused products, this approach is sufficient for our purposes.

Second, the broader vicarious calibration and cross-calibration have different spatial and temporal requirements for *in situ* data samples. The broader vicarious calibration generates standard gain factors to use for all locations across all dates. The scene-dependent cross-calibration for this study is focused on minimizing the  $nLw$  difference between the base sensor and the calibrated sensor on a coincident date to improve data fusion. Therefore, whereas the broader vicarious calibration uses individual *in situ* data samples from one or more stationary in-water sensors aggregated over many dates of imagery, the cross-calibration activity uses synthetic *in situ* data sampled at multiple locations within a single date of imagery.

Third, APS and SeaDAS both have options to use  $Lw$  or  $nLw$  as the *in situ* data type for the vicarious calibration. Due to differences between the normalization approaches for  $Lw$  used by the in-water sensors and APS, the broader vicarious calibration process will sometimes use  $Lw$  as the *in situ* data in the inverse pass and let APS perform its own normalization.<sup>15</sup> However, in this cross-calibration activity, the synthetic *in situ*  $nLw$  data from the base sensor and the calibrated sensor are both generated with the same APS normalization method. Therefore, the normalization method used for the synthetic *in situ* data (VIIRS) and calibrated data (MODIS) is consistent. Therefore, instead of using  $Lw$  as the *in situ* data, this cross-calibration approach used  $nLw$  as the *in situ* data in the inverse pass. This simplified the processing required and made it easier for the method to be adapted to an operational mode.

Finally, the broader vicarious calibration adjusts the gain factors for the NIR and visible wavelength bands separately. This is done because the NIR wavelength bands are used to generate the La values. The Gordon and Wang atmospheric correction algorithm<sup>18</sup> computes

atmospheric correction parameter measurements as a function of the ratio of the reflectance at the 748 to 869 nm wavelengths for selecting an aerosol model that characterizes the actual aerosol radiance contribution. The selected aerosol model indexed by these atmospheric correction parameters directly influences the  $La$  values that are used in Eq. (6) to compute the  $vLt$  values. Therefore, the broader vicarious calibration is first performed on the two NIR wavelength bands that are used to calculate  $La$ . Once the NIR wavelength gain factors are computed they are locked and used, whereas the vicarious calibration process is performed again to compute the gain factors for the visible wavelength bands.

Since  $nLw$  reflectance is small at the NIR wavelengths, any atmospheric contamination can impact the base sensor's NIR  $nLw$  estimate, causing it to deviate from the true measurement. Whereas these deviations in the  $nLw$  measurement can be small in absolute value, they can be significant in relative percent error terms and can impact the vicarious calibration adjustments of the NIR wavelength gain factors. Therefore, to create the most accurate standard NIR gain factors, the broader multiscene vicarious calibration uses samples drawn from preselected scenes which have the most pristine cloud-free atmospheric conditions possible and assumes that the scene is characterized by a thin aerosol model. Then, the inverse pass of the vicarious calibration for the NIR wavelength bands uses the  $La$  values associated with this thin aerosol model.

However, the cross-calibration methodology is a scene-dependent adjustment which is designed in part to overcome the differences and contamination caused by clouds, haze, and other effects. This process, by its very nature, will be performed on datasets that have potentially significant aerosols and do not have pristine atmospheric conditions. Therefore, no assumptions can be made about what initial aerosol model is appropriate to use for the  $La$  values in the vicarious calibration of the NIR wavelength bands. Therefore, this cross-calibration approach relies on the already established standard NIR gain factors of the calibrated sensor and only performs one vicarious calibration process, which is used to adjust the gain factors for the visible wavelength bands.

### 3.2 Processing Activity

Tables 2 and 3 show the gain settings of the nine MODIS VNIR bands for the two MODIS study areas. The "Standard" row shows the current standard MODIS gain settings. The "Cross-calibrated" row shows the adjusted MODIS gain factors generated through the cross-calibration process. Since the NIR gains are not adjusted, there is no difference in the standard and cross-calibrated gains for the 748 and 869 nm wavelength bands.

The gains for the Mississippi Bight and Chesapeake Bay scenes are graphically shown in Fig. 5. The black lines in the graph represent the standard MODIS gains. The thin red lines in Fig. 5(a) represent the cross-calibrated MODIS gains generated at the individual sample points in the Mississippi Bight scene. The bold red line represents the mean of these individual sample point gains, which identifies the cross-calibrated gains that were used to reprocess the

**Table 2** Gain tables for the Mississippi Bight MODIS scene from March 14, 2014.

Wavelength (nm)	412	443	488	531	547	667	678	748	869
Standard	0.9731	0.9910	0.9935	1.0002	0.9994	0.9996	0.9998	0.9989	1.0000
Cross-calibrated	0.9600	0.9779	0.9920	1.0061	1.0004	1.0061	1.0021	0.9989	1.0000

**Table 3** Gain tables for the Chesapeake Bay MODIS scene from May 17, 2013.

Wavelength (nm)	412	443	488	531	547	667	678	748	869
Standard	0.9731	0.9910	0.9935	1.0002	0.9994	0.9996	0.9998	0.9989	1.0000
Cross-calibrated	0.9404	0.9583	0.9835	1.0001	1.0007	1.0092	1.0067	0.9989	1.0000

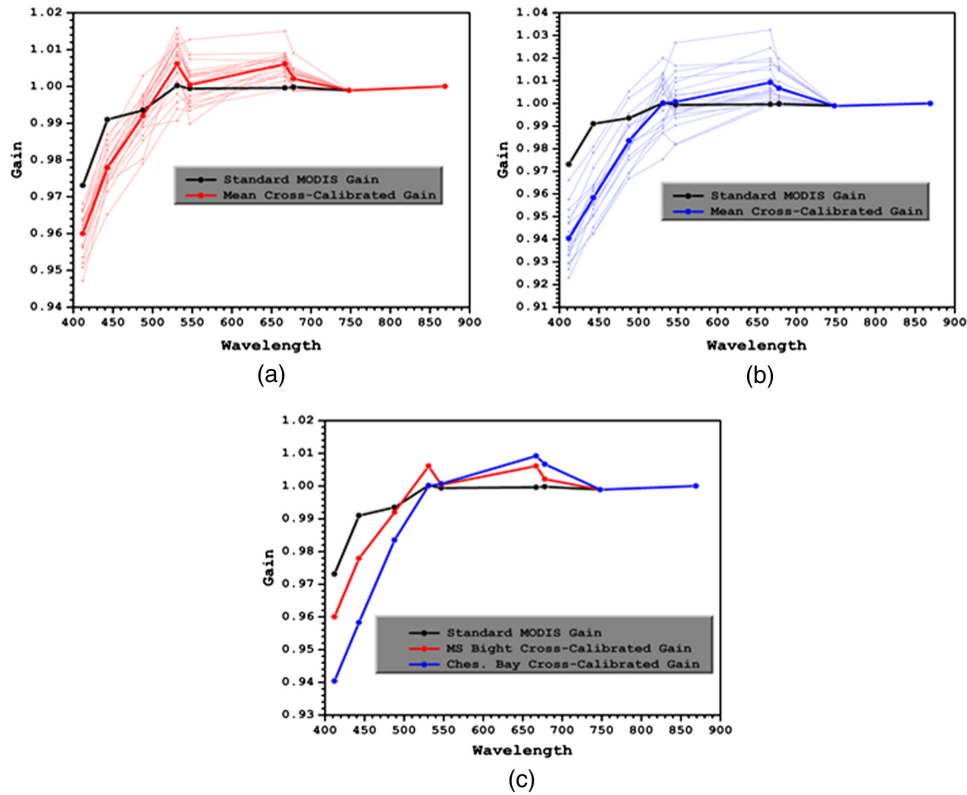


**Fig. 5** Spectral gains for (a) Mississippi Bight (b), Chesapeake Bay, and (c) Mississippi Bight and Chesapeake Bay.

Mississippi Bight MODIS scene. The thin blue lines in Fig. 5(b) represent the cross-calibrated MODIS gains generated at the individual sample points in the Chesapeake Bay scene. The bold blue line represents the mean of these individual sample point gains, which identifies the cross-calibrated gains that were used to reprocess the Chesapeake Bay MODIS scene.

The standard and cross-calibrated MODIS gains for the Mississippi Bight and Chesapeake Bay scenes are plotted together in Fig. 5(c). These gain differences show that for both scenes the cross-calibrated gains are lower than the standard gains through the blue wavelengths, but then are almost the same or slightly higher in the green and red wavelengths.

The MODIS scenes were reprocessed using their cross-calibrated gain settings. The residual mean square difference (RMSD) between the synthetic *in situ* VIIRS and MODIS *nLw* values at the sample points for the Mississippi Bight and Chesapeake Bay scenes is shown in Tables 4 and 5, respectively. In both cases, the most significant improvement in the matchup between the MODIS and VIIRS *nLw* data caused by the cross-calibration occurs in the blue wavelengths. The percent reduction in the RMSD between the VIIRS and MODIS *nLw* values for these 412, 443, and 488 nm wavelength bands resulting from the cross-calibration across these scene pairs is 61, 66, and 5% for the Mississippi Bight scene and 56, 57, and 27% for the Chesapeake Bay scene.

**Table 4** Mean *nLw* residual-mean square difference (RMSD) between VIIRS and MODIS at sample points for the Mississippi Bight scene.

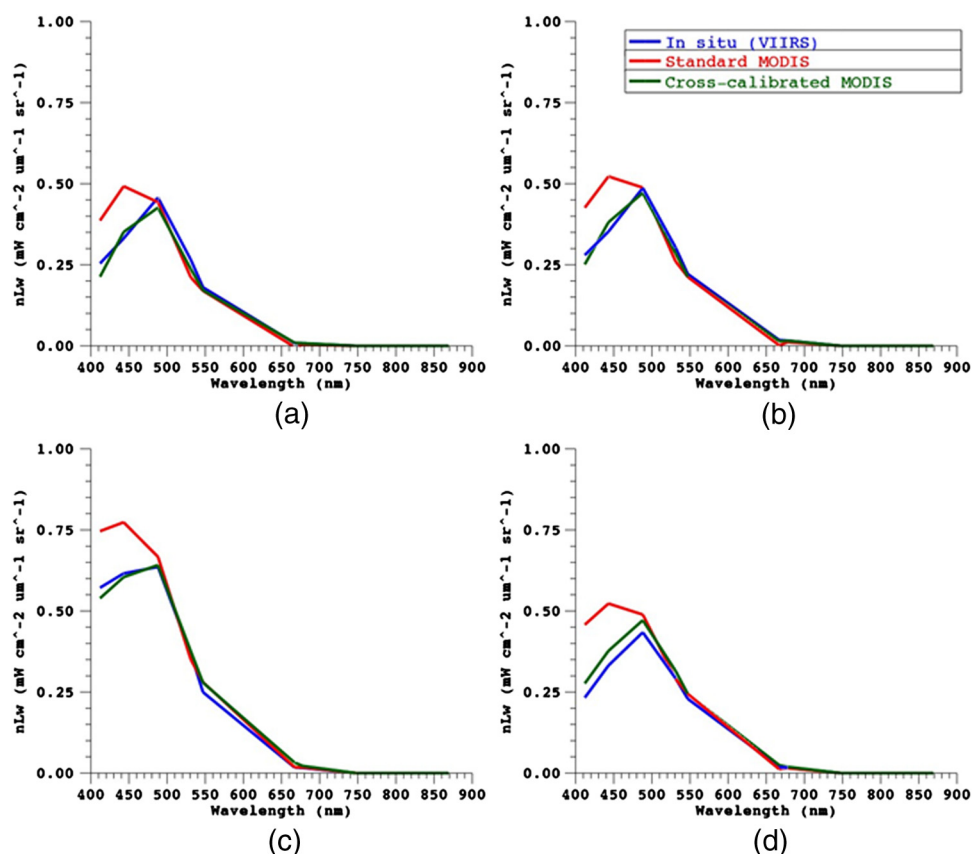
Wavelength (nm)	412	443	488	531	547	667	678
RMSD (Standard MODIS gains)	0.190	0.151	0.043	0.046	0.025	0.015	0.007
RMSD (Cross-calibrated MODIS gains)	0.075	0.052	0.041	0.036	0.024	0.006	0.005

**Table 5** Mean  $nLw$  RMSD between VIIRS and MODIS at sample points for Chesapeake Bay scene.

Wavelength (nm)	412	443	488	531	547	667	678
RMSD (Standard MODIS gains)	0.452	0.401	0.136	0.093	0.095	0.058	0.050
RMSD (Cross-calibrated MODIS gains)	0.200	0.174	0.099	0.068	0.067	0.047	0.045

Graphs of the VIIRS, standard MODIS and cross-calibrated MODIS  $nLw$  spectra at four selected sample points are shown in Fig. 6 for the Mississippi Bight scene and in Fig. 7 for the Chesapeake Bay scene. For these graphs, the VIIRS  $nLw$  spectra appear in blue, the standard MODIS  $nLw$  spectra are shown in red, and the cross-calibrated MODIS  $nLw$  spectra are presented in green. These graphs reveal the influence that the cross-calibrated gains had in lowering the MODIS  $nLw$  values in the blue wavelengths to more accurately approximate the VIIRS  $nLw$  values.

Plots of the chlorophyll value generated by the chl\_oc3 algorithm<sup>19,20</sup> for VIIRS, standard MODIS, and cross-calibrated MODIS are shown for the Mississippi Bight scene in Fig. 8(a) and the Chesapeake Bay scene in Fig. 8(b). In both cases, the  $x$ -axis represents the 20 *in situ* data sample locations, and the  $y$ -axis represents the chlorophyll values. The blue diamonds represent the VIIRS chlorophyll values. The red squares represent the standard MODIS chlorophyll values. The green dots represent the cross-calibrated MODIS chlorophyll values. Generally, the green dots representing the cross-calibrated MODIS chlorophyll values are closer to the blue VIIRS diamonds. In fact, in some cases, most of the blue VIIRS diamonds are hidden behind the green cross-calibrated MODIS dot, indicating that the cross-calibrated MODIS chlorophyll values very closely approximate the VIIRS chlorophyll values. These plots show that the

**Fig. 6**  $nLw$  spectral plots of VIIRS, standard MODIS and cross-calibrated MODIS for Mississippi Bight for (a) *in situ* location 3, (b) *in situ* location 5, (c) *in situ* location 9, and (d) *in situ* location 11.

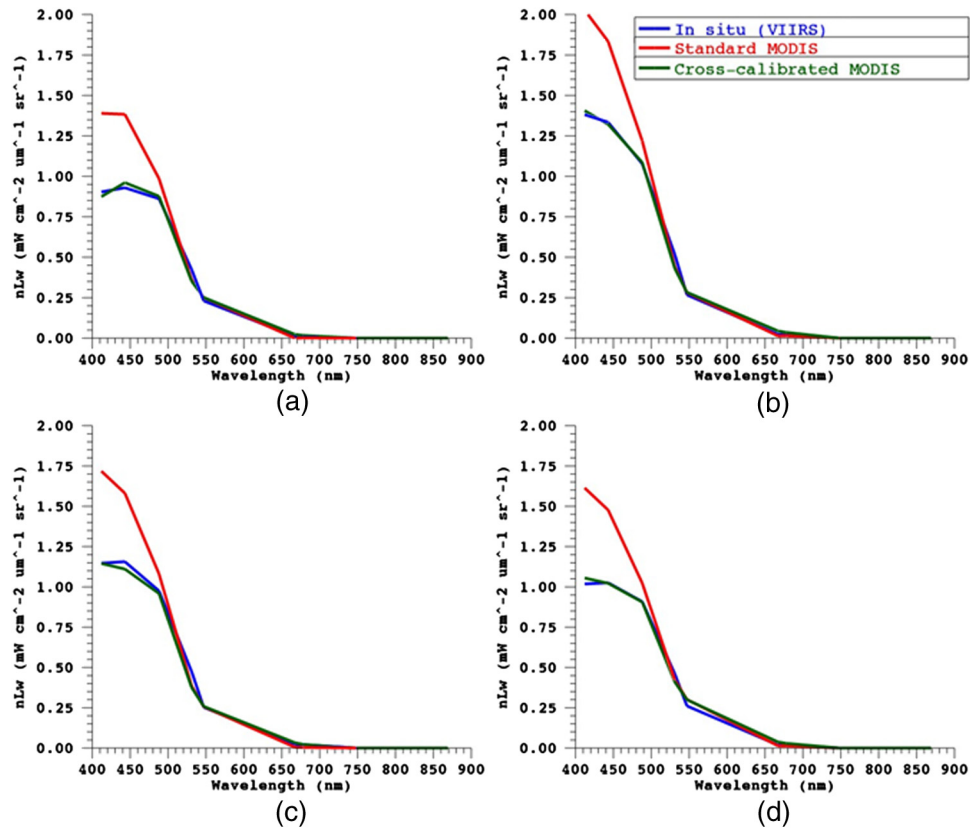


**Fig. 7**  $nLw$  spectral plots of VIIRS, standard MODIS and cross-calibrated MODIS for Chesapeake Bay for (a) *in situ* location 13, (b) *in situ* location 16, (c) *in situ* location 17, and (d) *in situ* location 18.

matchup between the VIIRS and MODIS chlorophyll values is improved by the cross-calibration.

For the Mississippi Bight scene, the RMSD between VIIRS and MODIS chlorophyll values over the sample points is  $0.117 \text{ mg/m}^3$  for the standard MODIS chlorophyll and  $0.069 \text{ mg/m}^3$  for the cross-calibrated MODIS chlorophyll. Therefore, the cross-calibration results in a 41% reduction in the RMSD between the VIIRS and MODIS chlorophyll estimates.

For the Chesapeake Bay scene, the RMSD between VIIRS and MODIS chlorophyll values over the sample points is  $0.470 \text{ mg/m}^3$  for the standard MODIS chlorophyll and  $0.145 \text{ mg/m}^3$

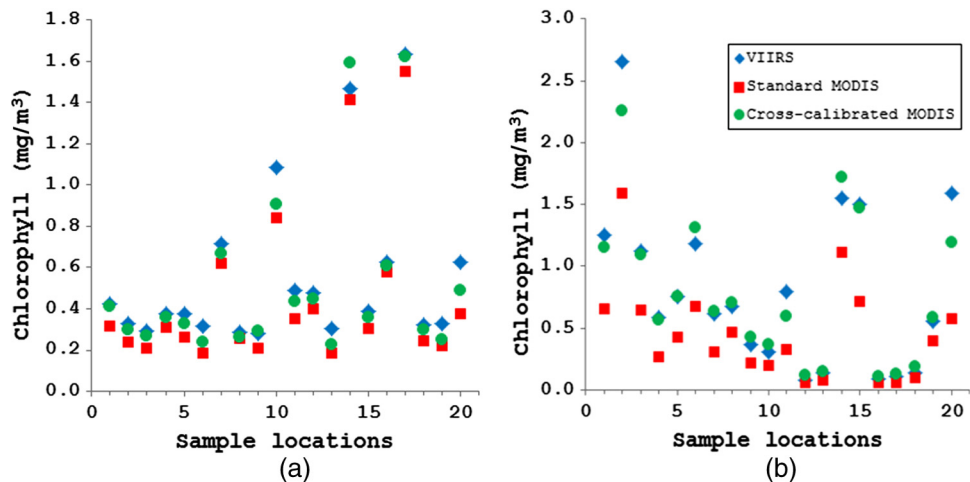


**Fig. 8** VIIRS, standard and cross-calibrated MODIS chlorophyll: (a) Mississippi Bight and (b) Chesapeake Bay.

**Table 6** Mississippi Bight RMSD between VIIRS and MODIS scene pairs at  $nLw$  wavelengths.

Wavelength (nm) or product	412	443	488	547	667	chl_oc3
RMSD (Standard MODIS gains)	0.314	0.274	0.128	0.082	0.041	2.052
RMSD (Cross-calibrated MODIS gains)	0.206	0.181	0.124	0.081	0.041	1.993

for the cross-calibrated MODIS chlorophyll. Therefore, the cross-calibration results in a 69% reduction in the RMSD between the VIIRS and MODIS chlorophyll estimates.

The tuning of the cross-calibrated MODIS gains is forced by the differences between the VIIRS and MODIS  $nLw$  values at the *in situ* locations. Outside these locations, across the scene extent, natural variability and water characteristics not presented at the *in situ* locations cause the RMSD between the aggregated VIIRS and MODIS  $nLw$  to be different than the RMSD of the  $nLw$  that exists at the *in situ* locations. However, improvement across the entire scene is essential to improving data consistency for data fusion.

To explore the effects of the cross-calibration across the entire scene, an intersection of all valid overlapping points between the VIIRS, standard MODIS, and cross-calibrated MODIS for each study area was generated for the blue through red wavelengths. Chlorophyll and  $nLw$  data were extracted from these intersecting points, and the RMSD between the VIIRS and standard MODIS values and the VIIRS and cross-calibrated MODIS values were generated. The RMSD between VIIRS and MODIS is shown in Table 6 for selected bands of the Mississippi Bight scene and in Table 7 for the same bands of the Chesapeake Bay scene.

Tables 6 and 7 indicate again that the more significant improvement derived from the cross-calibration for these datasets is in the 412, 443, and 488 nm wavelength bands, with a percent RMSD reduction of 34, 34, and 3% for the Mississippi Bight scene and a percent RMSD reduction of 29, 53, and 13% for the Chesapeake Bay scene across these wavelength bands. Therefore, whereas these  $nLw$  percent RMSD reductions are lower than the  $nLw$  percent RMSD reduction at the 20 sample points shown in Tables 4 and 5, the percent reduction in the  $nLw$  RMSD between VIIRS and MODIS across the valid overlapping pixels will still contribute to improving consistency in the VIIRS and MODIS  $nLw$  matchups, and their data fusion.

Scatter plots using the valid overlapping data between the VIIRS and standard MODIS scenes and also between the VIIRS and cross-calibrated MODIS scenes were created. Scatter plots of  $nLw$  data in Figs. 9 and 10, for the Mississippi Bight and Chesapeake Bay scenes respectively, are shown for the (a) 410, (b) 443, and (c) 486 nm wavelength bands of VIIRS on the  $x$ -axis with their associated MODIS wavelengths on the  $y$ -axis. The scatter plots of the associated VIIRS and MODIS chlorophyll values are shown in Figs. 9(d) and 10(d).

The VIIRS versus standard MODIS scatter plots are shown in red, while the VIIRS versus cross-calibrated MODIS scatter plots are shown in green. The red  $nLw$  scatter plots, centered above the one-to-one line, indicate the tendency for the MODIS  $nLw$  values in this scene pair to be higher than the VIIRS when the standard MODIS gains are used in processing. The green scatter plots, centered more closely to the one-to-one data line, represent the improvement in the MODIS alignment with VIIRS after the cross-calibrated gains are applied.

A qualitative visual assessment of the improvement resulting from the cross-calibration for the March 14, 2014 Mississippi Bight study area is shown in Fig. 11. Comparison of the standard MODIS chlorophyll product [Fig. 11(a)] with the VIIRS chlorophyll product [Fig. 11(c)] shows the improvement created by the cross-calibration when inspected beside the comparison of the cross-calibrated MODIS chlorophyll product [Fig. 11(b)] with the VIIRS chlorophyll product

**Table 7** Chesapeake Bay RMSD between VIIRS and MODIS scene pairs at  $nLw$  wavelengths.

Wavelength (nm) or product	412	443	488	547	667	chl_oc3
RMSD (Standard MODIS gains)	0.399	0.433	0.183	0.114	0.063	2.737
RMSD (Cross-calibrated MODIS gains)	0.282	0.205	0.160	0.121	0.067	2.592

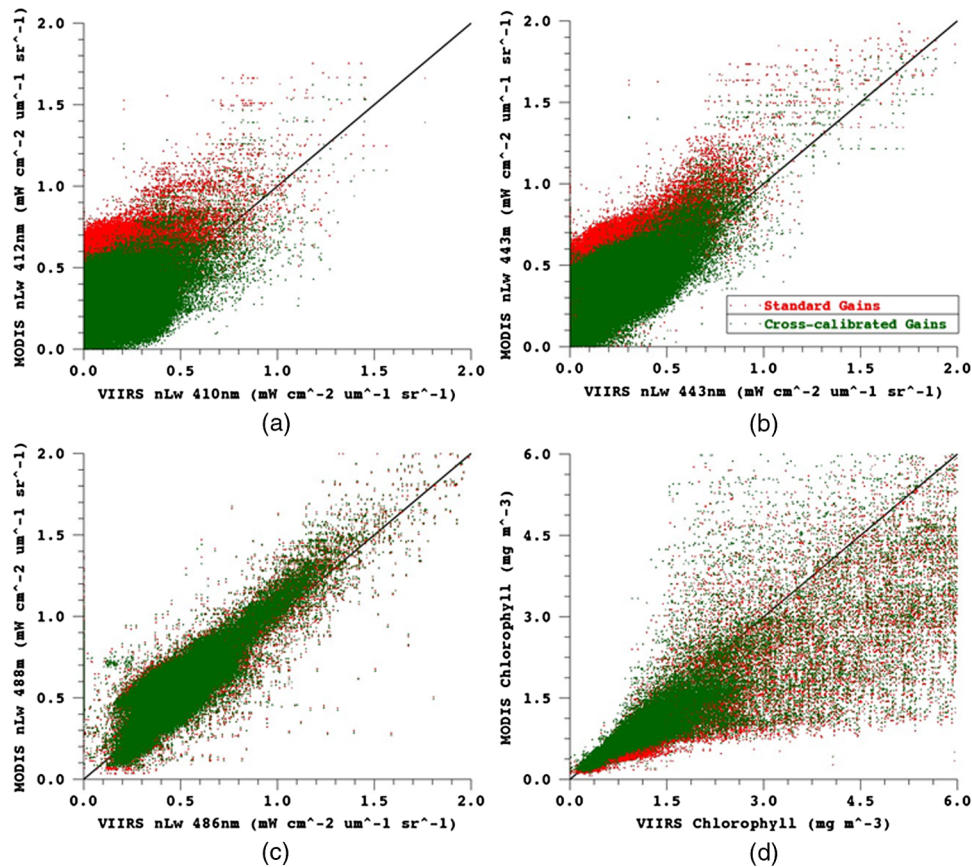


**Fig. 9** Mississippi Bight VIIRS versus MODIS scatter plots: (a) 410 nm *nLw*, (b) 443 nm *nLw*, (c) 486 nm *nLw*, and (d) chlorophyll.

[Fig. 11(c)]. The black shading along the lower-left section of the images near the mouth of the Mississippi River and along the Florida Panhandle indicates areas where clouds and atmosphere contaminate the scene. The left-most white circle south of the Mississippi Sound highlights one general area where clouds contaminate the VIIRS image. The right-most white circle south of Panama City, Florida, highlights another area where clouds contaminate the MODIS image.

The black circles highlight areas where the color levels show the standard MODIS chlorophyll image to deviate from the VIIRS image. The green patterns that appear in the black circles of the VIIRS image are almost completely replaced by blue color values in the standard MODIS image, indicating a reduction in the standard MODIS chlorophyll values from the VIIRS chlorophyll values. However, these green color patterns, discernible in the VIIRS chlorophyll image, do appear in the cross-calibrated MODIS chlorophyll image. This demonstrates the ability for the cross-calibration of the MODIS scene, using the VIIRS synthetic *in situ nLw* data, to adjust the MODIS chlorophyll values such that they are better aligned with the VIIRS chlorophyll values.

After the MODIS chlorophyll products for the Mississippi Bight were created, they were fused with the VIIRS chlorophyll product. At the locations where both scenes are cloud-free, the fusion process uses an average of the two sensor product values to generate the data value for the fused product. Where only one scene is cloud-free, the cloud-free sensor's product value is used as the data value for the fused product. The fused VIIRS and standard MODIS chlorophyll product [Fig. 11(d)] and the fused VIIRS and cross-calibrated MODIS product [Fig. 11(e)] can be compared to the VIIRS chlorophyll product [Fig. 11(c)]. The left-most white circle in both of the fused images identifies one location where the MODIS data filled in the black-colored cloud-covered VIIRS data. The right-most white circle in both of the fused images identifies one location where the VIIRS data filled in the black-colored cloud-covered MODIS data. The black circled areas identify locations where the color levels

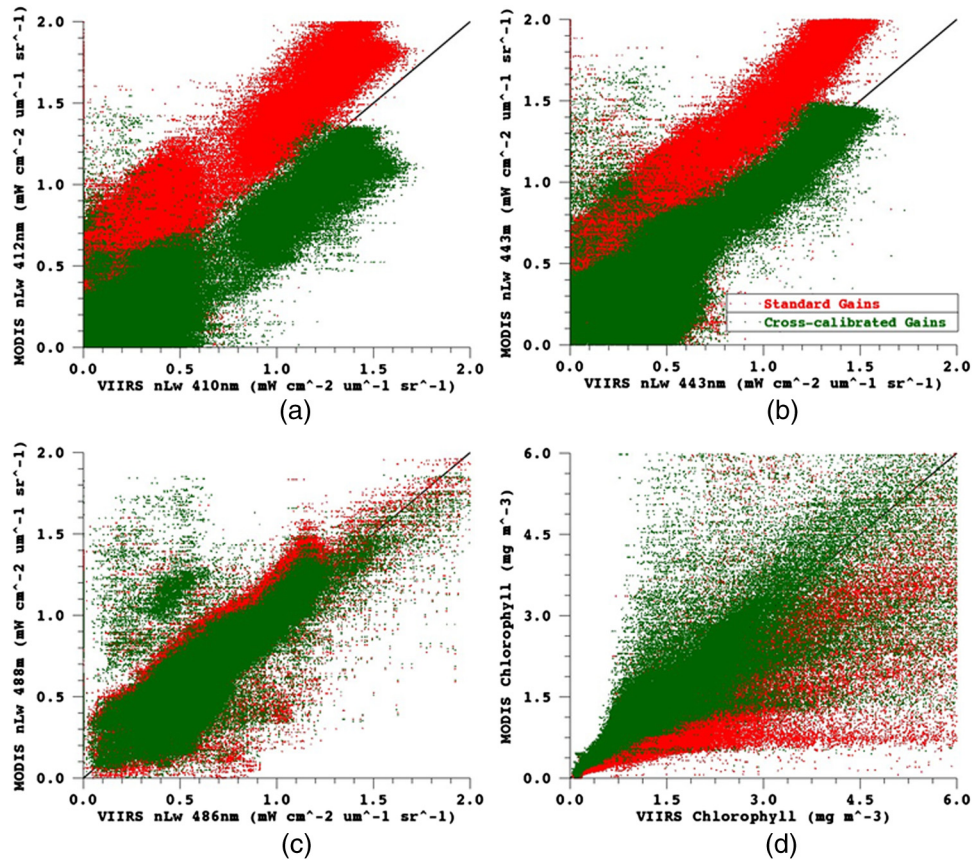


**Fig. 10** Chesapeake Bay VIIRS versus MODIS scatter plots: (a) 410 nm *nLw*, (b) 443 nm *nLw*, (c) 486 nm *nLw*, and (d) chlorophyll.

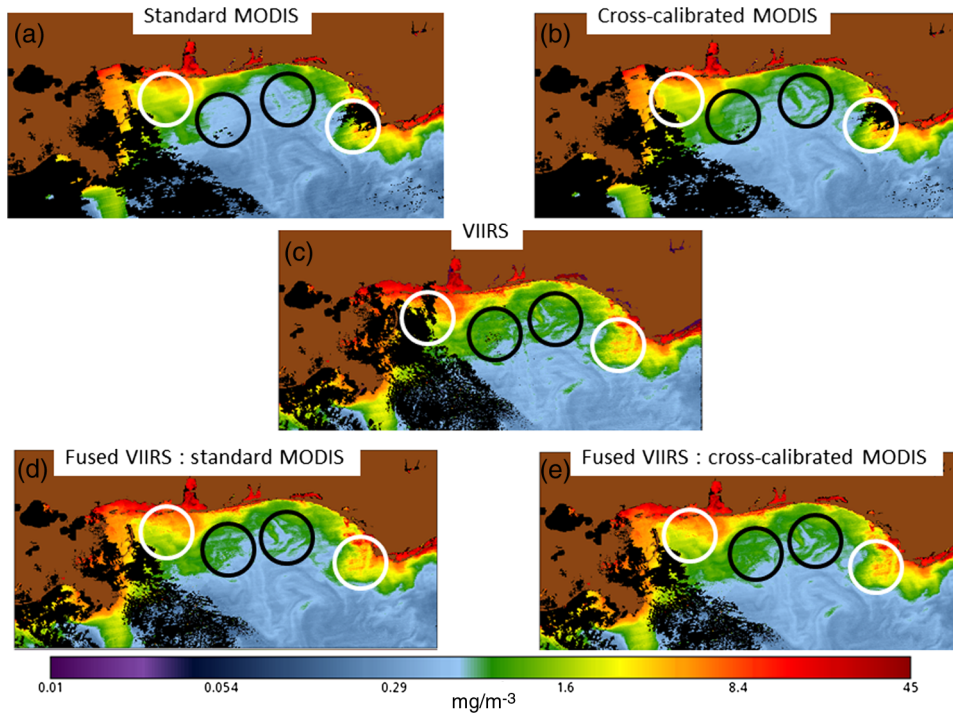


**Fig. 11** Mississippi Bight chlorophyll: (a) standard MODIS, (b) cross-calibrated MODIS, (c) VIIRS, (d) fused VIIRS and standard MODIS, and (e) fused VIIRS and cross-calibrated MODIS and VIIRS.

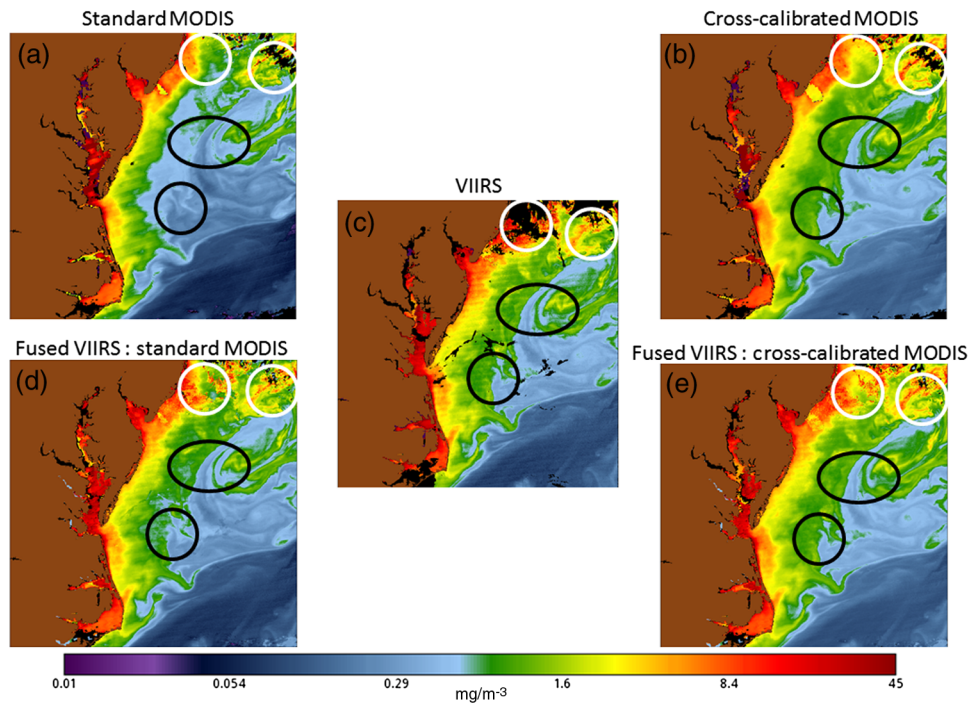


**Fig. 12** Chesapeake Bay chlorophyll: (a) standard MODIS, (b) cross-calibrated MODIS, (c) VIIRS, (d) fused VIIRS and standard MODIS, and (e) fused VIIRS and cross-calibrated MODIS.

representing chlorophyll estimates in the fused VIIRS and cross-calibrated MODIS chlorophyll image match the VIIRS chlorophyll image more closely when compared to the fused VIIRS and standard MODIS chlorophyll image.

A qualitative visual assessment of the improvement resulting from the cross-calibration for the May 17, 2013, Chesapeake Bay study area is shown in Fig. 12. Comparison of the standard MODIS chlorophyll product [Fig. 12(a)] with the VIIRS chlorophyll product [Fig. 12(c)] shows the improvement created by the cross-calibration when inspected beside the comparison of the cross-calibrated MODIS chlorophyll product [Fig. 12(b)] with the VIIRS chlorophyll product [Fig. 12(c)]. The black shading in these images also indicates areas where clouds and atmosphere contaminate this scene. The left-most white circle in these images highlights where clouds contaminate the VIIRS image off the New Jersey coast. The VIIRS image also has cloud

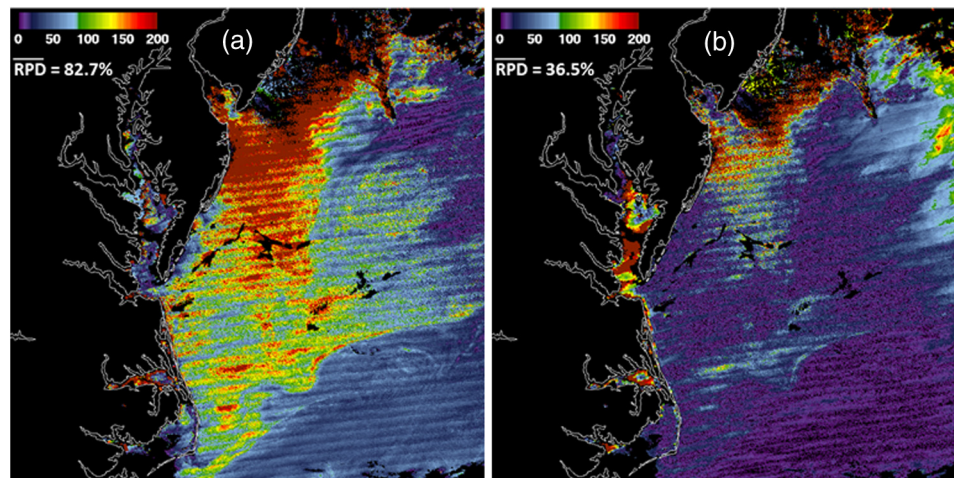


**Fig. 13** RPD images for 443 nm (a) VIIRS and standard MODIS and (b) VIIRS and cross-calibrated MODIS.

contamination across its center extending eastward from the mouth of the Chesapeake Bay and also over the waters of the North Carolina coast near the bottom of the image. The right-most white circle in the image highlights where clouds contaminate the MODIS image, also over the waters of the New Jersey coast.

The black circles highlight areas where the color levels show the standard MODIS chlorophyll image to deviate from the VIIRS image. As with the Mississippi Bight scene, the green patterns that appear in the black circles of the VIIRS image are almost completely replaced by blue color values in the standard MODIS image, indicating a reduction in the standard MODIS chlorophyll values when compared to the VIIRS chlorophyll values. However, these green color patterns, discernible in the VIIRS chlorophyll image, do appear in the cross-calibrated MODIS chlorophyll image. This provides additional evidence of the influence that the cross-calibration has on adjusting the MODIS chlorophyll values so that they are better aligned with the VIIRS chlorophyll values.

After the MODIS chlorophyll products for the Chesapeake Bay were created they were fused with the VIIRS chlorophyll product. The fused VIIRS and standard MODIS chlorophyll product [Fig. 12(d)] and the fused VIIRS and cross-calibrated MODIS product [Fig. 12(e)] can be compared to the VIIRS chlorophyll product [Fig. 12(c)]. The left-most white circle in both of the fused images identifies one location where the MODIS data filled in the black-colored cloud-covered VIIRS data. The right-most white circle in the fused images identifies one location where the VIIRS data filled in the black-colored cloud-covered MODIS data. The black circled areas identify locations where the color levels representing chlorophyll estimates in the fused VIIRS and cross-calibrated MODIS chlorophyll image match the VIIRS chlorophyll image more closely when compared to the fused VIIRS and standard MODIS chlorophyll image. Overall, these images show that, for this Chesapeake Bay VIIRS and MODIS scene pair, the cross-calibration and fusion process removed almost all of the clouds in the VIIRS scene while also providing more consistent VIIRS and MODIS data for the data fusion.

Images of relative percent difference (RPD) between the Chesapeake Bay VIIRS and MODIS  $nLw$  values at the 443 nm wavelength were produced following the equation:

$$nLw_{RPD}(\lambda) = \{abs[nLw_{VIIRS}(\lambda) - nLw_{MODIS}(\lambda)]\} / nLw_{VIIRS}(\lambda), \quad \text{for } \lambda = 443. \quad (11)$$

This was computed based on the VIIRS and standard MODIS  $nLw$  data [Fig. 13(a)] and also computed based on the VIIRS and cross-calibrated MODIS  $nLw$  data [Fig. 13(b)]. The yellow and red colors in Fig. 13(a) show that before cross-calibration there were significant differences between the two sensors in the  $nLw$  estimates at the 443 wavelength throughout much of the central section of the image. The image in Fig. 13(b) shows a drastic reduction in the RPD across the scene. Small areas where the RPD increased slightly after cross-calibration within the Chesapeake Bay may be due to haze that dominates the inshore area of the scene. There are still modest RPD values within the areas near the clouds at the top of the image, which is most likely due to the cloud adjacency effect. The off-shore increases in the RPD after cross-calibration shown in the extreme northeast of the image may be related to the cloud adjacency effect, but also may be due to insufficient allocation of sample points to drive the vicarious calibration in these areas.

These RPD products can serve as a tool to direct sampling locations for the vicarious calibration should time allow for a fine-tuning of the sample point selection in an operational mode. Overall, the mean RPD generated while using the VIIRS and standard MODIS  $nLw$  values was 82.7%, which is greater than the mean RPD of 36.5% generated while using the VIIRS and cross-calibrated MODIS  $nLw$  values. Also, the more homogeneous color coding of the RPD values after cross-calibration shows an improvement in the distribution of these RPD values over the scene extent. These reductions in the RPD realized through cross-calibration provide additional justification for performing the cross-calibration before fusing multisensor data products when inconsistencies are observed between the  $nLw$  estimates of the sensors used in the image fusion.

## 4 Conclusions

A cross-sensor calibration methodology using a vicarious calibration methodology was applied to Mississippi Bight and Chesapeake Bay VIIRS and MODIS scene pairs. Estimates of  $nLw$  from the VIIRS scene at 20 points for each scene pair were used as synthetic *in situ*  $nLw$  data for the cross-calibration of the MODIS scene. This generated cross-calibrated gains factors for the MODIS data which when applied to the MODIS  $Lt$  data produced derived  $nLw$  values that were in better agreement with the VIIRS derived  $nLw$  values.

This resulted in RMSD percent reductions between the VIIRS and MODIS  $nLw$  data at the 20 sample points of 61, 66, and 5% for the Mississippi Bight scene pair over the 412, 443, and 488 nm wavelength bands, respectively. The percent reduction in the RMSD after cross-calibration for all valid overlapping pixels in the Mississippi Bight VIIRS and MODIS scene pair for these same bands was 34, 34, and 3%.

There was a 56, 57, and 27% RMSD percent reduction between the VIIRS and MODIS  $nLw$  data at the 20 sample points in the Chesapeake Bay scene over the 412, 443, and 488 nm wavelength bands. The corresponding percent reduction in the RMSD for all valid overlapping pixels in the Chesapeake Bay VIIRS and MODIS scene pair for those same wavelength bands was 29, 53, and 13%. The cross-calibration resulted in a 3% reduction in the RMSD between the VIIRS and MODIS chlorophyll values for the Mississippi Bight scene and a 5% reduction for the Chesapeake Bay scene.

When scenes have cloud cover, the fusion between VIIRS and MODIS scenes can create an updated image with reduced cloud cover. The more consistent matchup between VIIRS and MODIS resulting from the cross-calibration led to a higher quality of data fusion. Since vicarious calibration can generate cross-calibrated gains which result in reducing the difference between MODIS and VIIRS  $nLw$  values at the *in situ* point locations, as well as reducing the  $nLw$  differences across the scene extent, it proves to be an important cross-sensor calibration method for adjusting remotely sensed data prior to data fusion. This cross-sensor calibration methodology can be used to improve the fusion between other current and future sensors.

## Acknowledgments

Funding for this work was provided by the Naval Research Laboratory (NRL) project, "Improving Blended Multi-Sensor Ocean Color Products through Assessment of Sensor Measurement Differences."

## References

1. NASA, "Moderate resolution imaging spectroradiometer," 2015, [modis.gsfc.nasa.gov](http://modis.gsfc.nasa.gov) (14 July 2015).
2. NASA, "Polar-orbiting missions: visible infrared imaging radiometer suite (VIIRS)," 2015, [npp.gsfc.nasa.gov/viirs.html](http://npp.gsfc.nasa.gov/viirs.html) (14 July 2015).
3. NASA, "Ocean color web: SeaWiFS," 2015, [oceancolor.gsfc.nasa.gov/cms/data/seawifs](http://oceancolor.gsfc.nasa.gov/cms/data/seawifs) (14 July 2015).
4. NASA, "Ocean color web: CZCS," 2015, [oceancolor.gsfc.nasa.gov/cms/data/czcs](http://oceancolor.gsfc.nasa.gov/cms/data/czcs) (14 July 2015).
5. NASA, "Ocean color web," 2015, [oceancolor.gsfc.nasa.gov/cms](http://oceancolor.gsfc.nasa.gov/cms) (14 July 2015).
6. S. Bailey et al., "Sources and assumptions for the vicarious calibration of ocean color satellite observations," *Appl. Opt.* **47**(12), 2035–2045 (2008).
7. E. J. Kwiatkowska et al., "Cross calibration of ocean-color bands from moderate resolution imaging spectroradiometer on terra platform," *Appl. Opt.* **47**(36) (2008).
8. M. Wang and B. Franz, "Comparing the ocean color measurements between MOS and SeaWiFS: a vicarious intercalibration approach for MOS," *IEEE Trans. Geosci. Remote Sens.* **38**, 184–197 (2000).
9. B. A. Franz et al., "Sensor-independent approach to the vicarious calibration of satellite ocean color radiometry," *Appl. Opt.* **46**, 5068–5082 (2007).
10. D. K. Clark et al., "MOBY, a radiometric buoy for performance monitoring and vicarious calibration of satellite ocean color sensors," Measurement and data analysis protocols, in

*Ocean Optics Protocols for Satellite Ocean Color Sensor Validation, Revision 4, Volume VI: Special Topics in Ocean Optics Protocols and Appendices*, J. L. Mueller, G. S. Fargion, and C. R. McClain, Eds., NASA Goddard Space Flight Center, Greenbelt, Maryland, NASA/TM2003-211621/Rev4-Vol.VI:3-34 (2003).

11. NASA, "Formation flying: the afternoon "A-Train" satellite constellation," 2003, [aqua.nasa.gov/sites/default/files/references/A-Train\\_Fact\\_sheet.pdf](http://aqua.nasa.gov/sites/default/files/references/A-Train_Fact_sheet.pdf) (14 July 2015).
12. NASA, "The afternoon constellation," 2012, [atrain.nasa.gov](http://atrain.nasa.gov) (14 July 2015).
13. ESA, "Earth online: Sentinel 3," 2015, [earth.esa.int/web/guest/missions/esa-future-missions/sentinel-3](http://earth.esa.int/web/guest/missions/esa-future-missions/sentinel-3) (14 July 2015).
14. A. Lyapustin et al., "Scientific impact of MODIS C5 calibration degradation and C6+ improvements," *Atmos. Meas. Tech.* **7**, 4353–4365 (2014)..
15. P. Martinolich and T. Scardino, *Automated Processing System User's Guide Version 4.2*, NRL, Washington, D.C. [http://www7333.nrlssc.navy.mil/docs/aps\\_v4.2/html/user/aps\\_chunk/index.xhtml](http://www7333.nrlssc.navy.mil/docs/aps_v4.2/html/user/aps_chunk/index.xhtml) (2011).
16. NASA, "Ocean Color SeaDAS," 2015, [seadas.gsfc.nasa.gov](http://seadas.gsfc.nasa.gov) (14 July 2015).
17. Z. Ahmad and R. S. Fraser, "An iterative radiative transfer code for ocean-atmosphere systems," *J. Atmos. Sci.* **39**(3), 656–665 (1982).
18. H. R. Gordon and M. Wang, "Retrieval of water-leaving radiance and aerosol optical thickness over the oceans with SeaWiFS: a preliminary algorithm," *Appl. Opt.* **33**(3) (1994).
19. J. E. O'Reilly et al., "2000: SeaWiFS postlaunch calibration and validation analyses," Part 3. NASA Technical Memorandum 2000-206892," Vol. **11**, p. 49, NASA Goddard Space Flight Center, Greenbelt, Maryland (2000).
20. M. J. Sauer et al., "Under the hood of satellite empirical chlorophyll a algorithms: revealing the dependencies of maximum band ratio algorithms on inherent optical properties," *Opt. Express* **20**(19), 20920 (2012).

**Mark David Lewis** is a researcher at the Naval Research Laboratory. He received his BS degrees in mathematics and computer science from the University of Oklahoma in 1982 and 1984, respectively. He received his MS degree in computer science from the University of Southern Mississippi (USM) in 1993 and his PhD degree in scientific computing from USM in 2000. His current interests include analysis of ocean color products derived from hyperspectral and multispectral remotely sensed data.

Biographies for the other authors are not available.